Geophysical Journal International

Porosity anisotropy of Opalinus Clay: implications for the poroelastic behaviour

Lukas M. Keller

University of Applied Sciences, 8400 Winterthur, Zürich, Switzerland. E-mail: kelu@zhaw.ch

SUMMARY
Regarding the storage of nuclear waste within clay rock formations, which are considered as natural seals, requires fundamental understanding of the poromechanical behaviour of this rock type with regard to the risk evaluation process. Here, the influence of pore fluid pressure on elastic properties of Opalinus Clay was studied on the basis of realistic pore microstructures, which were reconstructed from image data acquired by focused ion beam nanotomography. These microstructures were used as input pore geometries for linear elastic finite-element modeling in order to predict the anisotropic poroelastic properties of Opalinus Clay. The computational approach allowed determining complete sets of anisotropic poroelastic coefficients. It was found that the anisotropic pore structure of Opalinus Clay leads to a poroelastically anisotropic behaviour. In particular, the pore pressure affects vertical strain/stress differently when compared to the horizontal direction. Hence, long-term safety assessments related to a potential repository for nuclear waste within the Opalinus Clay unit should include anisotropic poroelasticity to predict the mechanical response of this geomaterial.

Key words: Microstructures; Permeability and porosity; Elasticity and anelasticity.

INTRODUCTION

Regarding the evaluation of clay rocks as potential host rocks for radioactive waste, a deeper understanding of their petrophysical and mechanical properties became increasingly important during recent years. In this study, the focus is on Opalinus Clay, which is considered as potential host rock for the storage of nuclear waste (Nagra 2002, 2004; Andra 2005). This rock formation varies in the relative contents of clay and non-clayey mineral grains, which affects petrophysical properties. Effective rock properties are controlled by the respective properties of the homogenous constituents and shales are often considered as a binary mixture of a porous clay matrix and non-clayey mineral grains. This simplification was made in terms of permeability (Revil & Cathles 1999), solute diffusion (Robinet *et al*. 2012; Keller *et al*. 2015) and also in terms of elastic properties (e.g. Sone & Zoback 2013). In the latter case, the clay matrix was considered as the 'soft' and non-clayey minerals as the 'stiff' end-members, respectively.

Clay rocks are characterized by a pronounced mechanical anisotropy, which is commonly attributed to the preferred orientation of platy clay minerals (Hornby *et al*. 1994; Johnston & Christensen 1995) and organic materials in case of organic-rich shales (Vernik & Nur 1992; Vernik & Liu 1997). Hence, it is the grain-preferred orientation related to the 'soft' clay matrix, which is supposed to determine the mechanical anisotropy of shales. Even if the clayey grains may appear well organized, geometric incompatibilities between individual grains after all exist, which leads to the

formation of predominantly nanoscale intergranular pores (Keller *et al*. 2013a). In addition to the preferred orientation of clay grains, the presence of an anisotropic pore space contributes to the overall mechanical anisotropy (Sarout & Gueguen 2008a,b; Sarout *et al*. 2014; Keller 2016).

Regarding shales, there is substantial interest in its anisotropy, in particular if there are fluids present in the pores. Fluids in form of gas can be found in pores of gas shales, which became increasingly exploited by the gas industry during recent years. On the other end of the spectrum of interest, aqueous pore fluids may facilitate radionuclide transport and thus, it is important to understand the role of pore fluids in influencing effective material properties of shales. In addition, it has been argued that the presence of an anisotropic porosity can influence the mechanical response (e.g. earthquake) of saturated rocks differently when compared to predictions made on the base of the conventional assumption of isotropic porosity (see Healy 2012 for further discussion).

In this work, we make an attempt to predict the influence of pore fluids on the elastic properties of Opalinus Clay. The aim is to determine numbers of anisotropic poroelastic constants by using the calculation scheme presented by Berryman (2010) that can be used in combination with given elastic constants of the porous media. Elastic constants of porous media can be determined experimentally or they can be calculated from realistic pore microstructures, which were reconstructed from tomographic image data (Garboczi 1998). Here, elastic constants were calculated by using finite-element modeling in combination with realistic pore microstructures, which were

reconstructed from image data acquired by focused ion beam nanotomography (FIB-nt).

METHODS

Calculation of poroelastic coefficients

It is assumed that the overall anisotropy related to the porous clay matrix is caused by a combination of preferred orientation of platy clay minerals as well as shape-preferred orientation of pores (Sarout & Gueguen [2008a,b]; Sarout *et al.* [2014]; Keller [2016]). In such a case, the anisotropy might be described by the orthorhombic version of the poroelastic equations (Berryman [2010])

$$\begin{pmatrix} e_{11} \\ e_{22} \\ e_{33} \\ -\zeta \end{pmatrix} = \begin{pmatrix} s_{11} & s_{12} & s_{13} & -\beta_1 \\ s_{21} & s_{22} & s_{23} & -\beta_2 \\ s_{13} & s_{23} & s_{33} & -\beta_3 \\ -\beta_1 & -\beta_2 & -\beta_3 & \gamma \end{pmatrix} \begin{pmatrix} \sigma_{11} \\ \sigma_{22} \\ \sigma_{33} \\ -p_f \end{pmatrix}. \tag{1}$$

The e_{ii} are the strains in $i = 1, 2, 3$ directions, whereas the 1, 2 directions define the bedding plane and the 3 direction is perpendicular to bedding. The σ_{ii} are the corresponding stresses and p_f is the pore pressure. ζ is the incremental fluid mass flow out of the sample and $s_{ij} = s_{ij}{}^d$ are the drained compliances.

Constant

$$\beta_i = s_{i1} + s_{i2} + s_{i3} - \frac{1}{3\overline{K_i^g}} \tag{2}$$

relates p_f with e_{ii} and accounts for the poroelastic anisotropy of the material under consideration.

In case the porous skeleton behaves anisotropic, Berryman ([2010]) defined three directional grain bulk moduli as

$$\frac{1}{3\overline{K_i^g}} = s_{i1}^g + s_{i2}^g + s_{i3}^g, \tag{3}$$

where s_{ij} are the compliances related to the porous skeleton.

Coefficient γ relates p_f with ζ and is given as

$$\gamma = \frac{\beta_1 + \beta_2 + \beta_3}{B} = \frac{\alpha_R}{K_R^d B}, \tag{4}$$

where B is the Skempton ([1954]) coefficient. According to Berryman ([1997]), Skempton's B coefficient is given by

$$B = \frac{1 - \frac{K_R^d}{K_R^u}}{1 - \frac{K_R^d}{K_R^g}} = \frac{1 - \frac{K_R^d}{K_R^u}}{\alpha_R}, \tag{5}$$

where K_R^d and K_R^u are the Reuss ([1929]) average drained and undrained bulk moduli and K_R^g is the Reuss average bulk modulus of the porous skeleton (see below). For example, the drained Reuss average bulk modulus is defined by

$$\frac{1}{K_R^d} = \sum_{i,j=1,2,3} s_{ij}^d. \tag{6}$$

Finally, the Reuss effective stress coefficient is given by (Berryman [2010])

$$\alpha_R = 1 - \frac{K_R^d}{K_R^g}. \tag{7}$$

The effect of pore pressure p_f on shear strain (e.g. e_{12}) is excluded from the discussion because the non-orthotropic terms in the compliance matrix are small and are thus neglected. For orthotropic materials, we have $\beta_{ij} = 0$ and the pore pressure is not coupled with shear strain (see also Cheng [1997]).

Given the above equations, the calculation of the complete set of poroelastic coefficients requires the knowledge of the drained S^d and undrained S^u compliance matrices. These matrices in turn can be determined in the base of tomographic image data in combination with voxel-based FEM simulations.

Calculation of the compliance matrix

A voxel-based FEM implementation was used to calculate the elastic properties (Garboczi [1998]; see Madadi *et al.* [2009] for an overview). The approach was successfully applied to Fontainebleau sandstone in order to calculate elastic properties related to drained (dry), undrained (water saturated) and oil saturated conditions (Arns *et al.* [2002]). The applied method was exclusively developed for the use in combination with image data (e.g. tomographic data). Garboczi ([1998]) provides a comprehensive description of the modeling approach as applied to 3-D digitized images, using a conjugate-gradient algorithm to solve the discretized set of equations. In order to find the elastic moduli of the porous clay microstructure, a fixed applied strain are applied and periodic boundary conditions are assumed for the pore microstructures. Pores, which cross the boundaries of the system, are not a problem because periodic boundary conditions are known to reduce boundary artefacts particular in cases were computer simulation involve grains or pore objects as in the present case. The numerical solution for the displacement is found by minimizing the global linear elastic-free energy and the elastic moduli were obtained from the average stress found in the problem. The elastic deformation is calculated for each voxel and the average stress per voxel is computed and averaged over the entire microstructure, which yielded the effective elastic properties of the porous material.

The generalized Hooke's law for anisotropic materials may be written as:

$$\begin{pmatrix} \varepsilon_{xx} \\ \varepsilon_{yy} \\ \varepsilon_{zz} \\ 2\varepsilon_{yz} \\ 2\varepsilon_{zy} \\ 2\varepsilon_{xy} \end{pmatrix} = \begin{pmatrix} S_{11} & S_{12} & S_{13} & S_{14} & S_{15} & S_{16} \\ S_{21} & S_{22} & S_{23} & S_{24} & S_{25} & S_{26} \\ S_{31} & S_{32} & S_{33} & S_{34} & S_{35} & S_{36} \\ S_{41} & S_{42} & S_{43} & S_{44} & S_{45} & S_{46} \\ S_{51} & S_{52} & S_{53} & S_{54} & S_{55} & S_{56} \\ S_{61} & S_{62} & S_{63} & S_{64} & S_{65} & S_{66} \end{pmatrix} \begin{pmatrix} \sigma_{xx} \\ \sigma_{yy} \\ \sigma_{zz} \\ \sigma_{yz} \\ \sigma_{zy} \\ \sigma_{xy} \end{pmatrix}, \tag{8}$$

where S_{ij} is the representation of the compliance tensor, which linearly relates the six strain components with the six stress components. The aim of the FEM simulations is then to calculate an effective S_{ij} which correspond to a given porous clay rock microstructure. In order to determine all elements of S_{ij}, one must execute six simulation runs while setting one after the other one of the six strain components to a non-zero value (Meille & Garboczi [2001]). In combination with the calculated average stress σ_{ij}, one can then define a system of equations that allows solving for the 36 unknowns in S_{ij}.

Errors associated to the calculation of the compliances

In an attempt to evaluate the contribution of shape-preferred orientation of pores on the overall elastic anisotropy of Opalinus Clay, Keller (2016) calculated drained and undrained compliance matrices using the same pore microstructure as in this study. This author also discussed in detail the errors that can be expected for this type of calculations and therefore, only a short summary is given here. Three types of errors were considered: (i) the deviation of the stiffness matrix $C = S^{-1}$ from symmetry, (ii) the discretization error and (iii) the finite size error.

(i) An elastic modulus should be symmetric for infinite systems as required by the theory of elasticity. The absolute value of the largest element of the antisymmetric part of C was considered as the error C_{err} on the determination of C and is defined as $C_{err} = |\max\{0.5(C\text{-}C^T)\}|$ (in units of GPa). C_{err} turned out to be small and the error related to deviations from symmetry was neglected.

(ii) The discretization error is related to the fact that the continuous pore space is represented by a finite number of discrete cubes (i.e. voxels). By a systematic variation of the image resolution, the discretization error on the determined elastic moduli can be evaluated (see also Roberts & Garboczi 2000). For the resolution used in this study, the relative discretization error is on the order of a few percent (see Keller 2016).

(iii) Elastic properties where calculated from tomographic data, which are related to typical FIB-nt sample cubes with edge length of 5–10 µm. For such small sample sizes, the existence of spatial microstructural heterogeneities leads to uncertainties in the determined elastic properties. This problem is related to the concept of the representative volume element. These uncertainties were estimated from a statistical analysis (Kanit *et al*. 2003; Keller 2016). It turned out that for a sample size of 100^3 voxels, the relative error on the Voig–Reuss–Hill average bulk modulus related to solid clayey matrix is around 10 per cent, which is accepted here.

Resolution limitation of FIB: prediction of poroelastic coefficients as a function of porosity

The intergranular porosity of the total analysed volume (Figs 1b and c) is 3.05 vol. %. This is the porosity related to pore radii >5 nm, which can be resolved by FIB-nt. By including smaller pores as the one that can be resolved by FIB-nt, the total intergranular porosity in sample BDR is at least as high as 10 vol. % as it was determined from nitrogen adsorption analysis (Keller *et al*. 2011). Based on analysing the connectivity pores, Keller *et al*. (2013b) suggested full connectivity of the total intergranular pore space of Opalinus Clay. Therefore, it is assumed that the water can be drained completely from the pore space and that the drainable volume is at least about 10 vol. %.

Considering only the small fraction of 20–30 per cent of the total porosity that can be resolved by FIB-nt likely leads to unrealistic predictions of poroelastic properties. In order to estimate poroelastic properties up to the expected intergranular porosity range of 10–20 vol. %, the results from subsampling were analysed (Keller 2016). Subsampling means that the total analysed volume is broken up into a grid of cells (subsamples) and the compliance matrices are determined for each cell. The data set related to a cell size of $L = 100$ pixels covers a porosity range up to around 10 vol. % and the cell size is large enough such that the discretization error is acceptable (see Keller 2016). Therefore, this data set was used to determine the relation between porosity and elastic properties in the
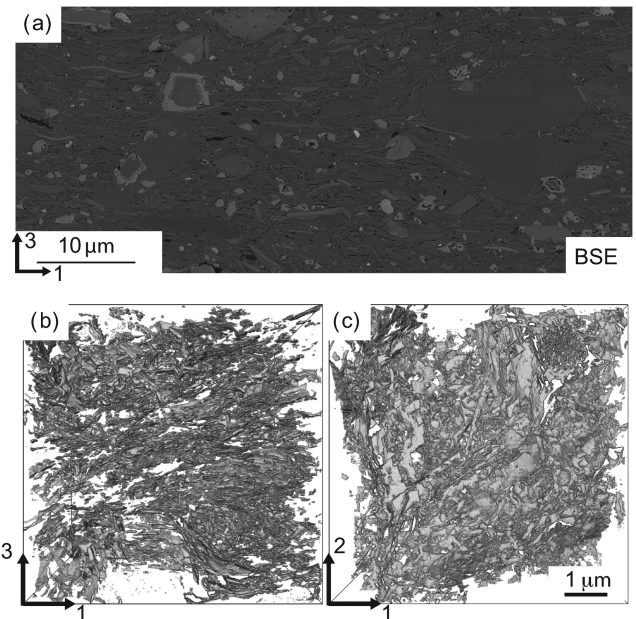

Figure 1. Backscatter electron (BSE) image and reconstructed pore microstructure of the investigated sample. Note, that the bedding plane is parallel to the 1–2 plane. (a) BSE image shows a cross-section trough the sample perpendicular to the bedding plane. (b) 1–3 view of the pore microstructure shows the anisotropy in the pore space. (c) 1–2 view of the pore microstructure.

0–20 vol. % porosity range. For each of the 125 cells, the porosity along with the poroelastic properties was calculated (see below).

Elastic properties of the solid porous skeleton

To perform simulations the elastic properties of the solid clay matrix must be defined. In order to consider the anisotropy related to the preferred orientation of clay platelets we assume that the porous solid behaves transversely isotropic. Wenk *et al*. (2008) provide transversely isotropic elastic constants related to the porous solid of Opalinus Clay. Elastic stiffness of these data was considered as unrealistic high (Wenk *et al*. 2008) but the data were used to calculate Thomsen's anisotropy parameters ε_s, γ_s and δ_s of the porous solid (Thomsen 1986; Table 1). Here, the values of these parameters were used in combination with realistic *P*- and *S*-wave velocities (V_p and V_s) and estimates on the dry bulk density (ρ) allowed assessing the constants of the stiffness tensor related to the porous solid using the following relations: $C_{33} = \rho V_p^2$, $C_{44} = \rho V_s^2$, $C_{66} = C_{44}(2\gamma + 1)$, $C_{11} = C_{33}(2\varepsilon + 1)$, $C_{12} = C_{11}-2C_{66}$, $C_{13} = \sqrt{a}-C_{44}$, where $a = \delta(2C_{33}(C_{33}-C_{44})) + (C_{33}-C_{44})^2$ (Thomsen 1986) (Table 1).

Values of Thomsen's parameters reported by Wenk *et al*. (2008) are generally lower than the ones obtained from wave velocity experiments (Sarout *et al*. 2014). This supports the hypotheses that in addition to textural-related, other microstructural factors (e.g. anisotropy in pore space) contribute to the elastic anisotropy. In addition, the Thomsen parameters related to textural factors are similar to the one obtained at the highest confining pressure in wave velocity experiments (Sarout *et al*. 2014). This fact and because the pores at the highest applied confining pressure are expected to be closed (Sarout *et al*. 2014) makes us confident that the used Thomsen parameters (Table 1) are largely controlled by the texture of the minerals.

Table 1. Properties of the porous solid skeleton.

ε_S	γ_S	δ_S	Vp normal to bedding (km s^{-1})	Vs normal to bedding (km s^{-1})	ρ bulk dry (kg m^{-3})	C_{11} (GPa)	C_{33} (GPa)	C_{13} (GPa)	C_{44} (GPa)	C_{66} (GPa)	$K_R{}^g$ (GPa)
0.28[1]	0.21[1]	0.17[1]	2.62[2]	1.51[2]	2310[3]	24.77[4]	15.86[4]	7.70[4]	5.26[4]	7.47[4]	12.1[4]

Based on data from [1] Wenk *et al.* (2008), [2] Bock (2001), [3] Nagra (2002), [4] This study.

Using the tabulated elastic constants, the Reuss averaged bulk grain modulus $K_R{}^g$ is about 12 GPa. Values of elastic properties related to the solid clay matrix have been experimentally determined by Vanorio *et al.* (2003), who obtained values for the bulk modulus ranging between 6 and 12 GPa and values for the shear modulus ranging between 4 and 6 GPa. This value range is consistent when compared to results obtained on the nanometer scale using atomic force acoustic microscopy, which yielded values for the Young's modulus of 6.2 GPa (Prasad *et al.* 2002). The values used in this study fall in the range of experimentally derived values and hence are reasonable.

Input microstructures

The investigated microstructure is related to sample BDR, which was taken from the shaley facies of the Opalinus Clay (Fig. 1). On the microscopic scale, the backscatter electron image depicted in Fig. 1(a) shows that the investigated sample is composed of a fine-grained clay matrix and within this matrix there are numerous isolated non-clayey mineral grains. FIB-nt was applied to the sample and tomographic image data was collected, which allowed reconstructing the pore microstructure (Figs 1b and c). The voxel size was 10 nm and the size of the analysed volume comprised 567^3 voxels, which corresponds to an edge length of 5.67 µm. For more information on the sample properties, tomographic methods and image processing the reader is referred to Keller *et al.* (2013a,b).

From visual inspection, it is obvious that the resolved pores space is anisotropic and consists of numerous isolated and disk-like pore objects. Keller (2016) quantified the geometric anisotropy of the pore space by calculating the shape eigenaxes of the pore objects. It turned out that pore space is anisotropic and that pores in shales can be described as oblate spheroids, which are aligned in the plane of symmetry of the transverse isotropic matrix material.

RESULTS

For porosities up to 0.1, $K_R{}^u$ and $K_R{}^d$ decrease linearly with increasing porosity and thus, a linear model was fitted to the data to predict the Reuss average bulk moduli towards higher porosities (Fig. 2a). Fitting parameters are tabulated in Table 2. By assuming that the intergranular porosity of Opalinus Clay ranges between 0.1 and 0.15, the calculations predict that drainage of water reduces the Reuss average bulk moduli by about 35 per cent up to 55 per cent.

The behaviour of α_R and B in regard to their dependency on porosity is documented in Fig. 2(b). α_R increases linearly with increasing porosity and thereby reaches values of 0.47 up to 0.70 for porosities ranging between 0.1 and 0.15 (Fig. 2b). Again a linear model was fitted to the calculated values of α_R. According to eq. (5), B approaches the value of one for higher porosities but is undetermined for $\phi = 0$. The values of B that were obtained from simulations scatter between 0.45 and 0.8 but there is a tendency that

B increases with increasing porosity. To predict the values of B as a function of porosity, B values were calculated by using the linear models related to $K_R{}^u$, $K_R{}^d$ and α_R in combination with eq. (5). The result is the blue stippled line in Fig. 2(b) and it can be seen that B approaches the value of one for $\phi > 0.2$. For the expected porosity range of 0.1–0.15, predicted values of B range between 0.7 and 0.8.

To predict the behaviour of the γ coefficient, the linear models related $K_R{}^u$, $K_R{}^d$ and α_R, were used in combination with eqs (4) and (5). The resulting model is the stippled black line in Fig. 2(c) and it can be seen that coefficient γ depends strongly on ϕ (Fig. 2c). Regarding poroelastic behaviour, we find the relation $\beta_1 \approx \beta_2 < \beta_3$, which reflects the influence of the anisotropy and implies that Opalinus Clay is poroelastically anisotropic (=pore pressure affects normal stresses differently) (Fig. 2c). $K_R{}^d$ decreases linearly with porosity, which in combination with eq. (4) suggests that the β_i coefficients behave non-linear. Therefore, a power function was fitted to the β_i values, which were obtained from the FEM simulations (Fig. 2c and Table 2).

DISCUSSION

So far, there are no specific experimental studies, in which the poroelastic coefficients of Opalinus Clay were studied in detail. Given its potential use as a host rock in a repository for nuclear waste it is, however, critical to understand the poroelastic behaviour of this material in some detail. In this paper, we used realistic pore microstructures in combination with finite-element modeling in order to predict changes in poroelastic behaviour due to variations in porosity. An increasing confining pressure likely leads to an increasing extend of collapsed pores and thus, to a porosity reduction towards higher pressures. It should be noted that pore collapse could cause non-linear volumetric deformation effects (Detournay & Cheng 1993), which are not necessarily taken into account by setting the low porosity pore microstructures equal to the collapsed pore microstructure. Hence, with respect to the variation of poroelastic coefficients due to changes in confining pressure, the presented results should be considered as an approximation. The presented approach of analysing the elastic response due to changes in pore fluid pressure predicts that Opalinus Clay behaves poroelastically anisotropic as indicated by the relation $\beta_1 \approx \beta_2 < \beta_3$, which is caused by a geometric anisotropy in pore space (Fig. 2c, Keller 2016). Hence, pore fluid pressure affects vertical elastic strain (say in direction perpendicular to bedding) differently when compared to the directions parallel to bedding.

Fig. 2(a) reveals that differences in porosity affect elastic properties, which among others might be the cause of differences in elastic properties between different clay rocks or different samples. This may produce a spread in B and α_R values, which may indeed be the case in the experimental work on Opalinus Clay rocks of Jahns (2013), where B values between 0.55 and 0.95 were obtained. Interestingly, this is about the spread in B values that is predicted for
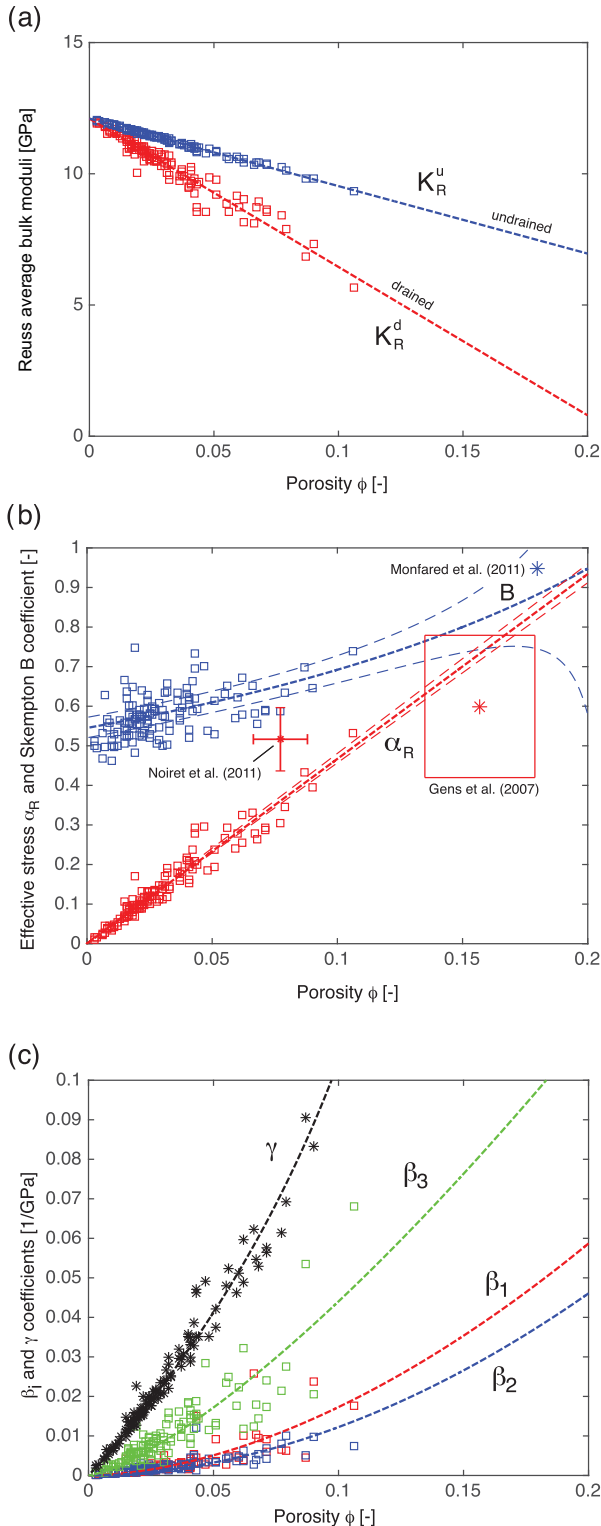
Figure 2. Values of poroelastic coefficients versus porosity. Markers show results from elastic simulations and the stippled lines are the fit of model functions to the data (see Table 3). (a) Reuss average drained (K_R^d) and undrained (K_R^u) bulk moduli versus porosity. (b) Reuss average effective stress coefficient α_R and Skempton's B versus porosity. Fine stippled marks mark the 95 per cent confidence interval. Asterisks mark experimentally derived values. The red rectangle marks the data range given by Gens *et al.* (2007). The red asterisks in the centre of the rectangle marks the reference value proposed by Gens *et al.* (2007) (see the text for further information). (c) γ and β_i coefficients versus porosity.

Table 2. Fitting parameter related to curves depicted in Fig. 2.

Parameter	Fitted function	R^2
K_R^u	$K_R^u = -56.52\phi + 12.1$	0.93
K_R^d	$K_R^d = -25.71\phi + 12.1$	0.99
α_R	$\alpha_R = 4.67\phi$	0.93
β_1	$\beta_1 = \phi^{1.76}$	0.58
β_2	$\beta_2 = \phi^{1.91}$	0.44
β_3	$\beta_3 = \phi^{1.36}$	0.74
γ	Use functions for K_R^u, K_R^d and α_R in combination with eqs (4) and (5)	–
B	Use functions for K_R^u, K_R^d and α_R in combination with eq. (5)	–

a porosity ranging from a few volume percent up to 20 vol. %. Cook (1999) reported even a higher spread in B values for an experiment where the effective pressure was successively increased. Thereby, B values decreased from values near 0.9 at low pressures to values of about 0.3 at high effective pressures. During this experiment, some fluid was drained from the sample during the incremental pressure increase. Hence, it is possible that the solid matrix stiffened, for example through the collapse of air-filled pores, which according to Fig. 2(b) leads to a decrease of the B values. Regarding these experiments, an additional decrease of the B values might be caused by the presence of very small quantities of air, which increases the fluid compressibility.

Next, the predicted values of poroelastic coefficients are compared to experimentally derived values. For this comparison we considered references, which provided also information on the porosity of the investigated samples (Fig. 2b). Monfared *et al.* (2011) obtained $B \approx 0.95$ at a porosity of about 0.18 using a hollow cylinder device. This value is in line with the model predictions and lies within the error bounds related to the predicted B values (Fig. 2b). Gens *et al.* (2007) presented reference values for Biot's effective stress coefficient ranging between 0.42 and 0.78 at a porosity of 15.7 ± 2.2 vol. %. Noiret *et al.* (2011) determined values of the Biot's effective stress coefficient for the Tournemire argillite and obtained a mean value of 0.52 at a mean porosity of about 7.7 vol. % (Fig. 2b). The model predictions lie between these two experimental values, which is considered as rough agreement. However, only a few data on poroelasticity coefficients of Opalinus Clay are available and the suitability of the predictive property of the presented model cannot be resolved finally at the presented state. Nevertheless, the presented model gives insight into the poroelastic behaviour of Opalinus Clay.

CONCLUSIONS

A computational approach that uses realistic pore microstructures of shales as input for finite-element modeling was used to predict the poroelastic behaviour of Opalinus Clay. It is predicted that Opalinus Clay behaves poroelastically anisotropic, which is controlled by the anisotropy of the pore space. In particular, pore fluid pressure affects vertical elastic behaviour differently when compared to the horizontal behaviour. Among others, this finding may have implications on the geomechanical response of Opalinus Clay in the event of, for example, an earthquake. Consequently, predictions on the geomechanical response related to this rock unit should consider anisotropic poroelasticity. Furthermore, in future experimental work on Opalinus Clay focus should be on the determination of anisotropic poroelastic coefficients.

ACKNOWLEDGEMENTS

REFERENCES

Andra, 2005. 'Dossier 2005 Argile—evaluation de la faisabilité du stockage géologique en formation argileuse profonde—Rapport de synthèse'. Andra, France. Available at: http://www.Andra.fr (2005 Juin).

Arns, C.H., Knackstedt, M.A., Pinczewski, W.V. & Garboczi, E.J., 2002. Computation of linear elastic properties from microtomographic images: methodology and agreement between theory and experiment, *Geophysics,* **67,** 1396–1405.

Berryman, J.G., 1997. Transversely isotropic elasticity and poroelasticity arising from thin isotropic layers, in *Theoretical and Computational Acoustics*, pp. 457–474, eds Teng, Y.-C., Shang, E.-C., Pao, Y.-H., Schultz, M.H. & Pierce, A.D., World Scientific.

Berryman, J.G., 2010. Poroelastic measurement schemes resulting in complete data sets for granular and other anisotropic porous media, *Int. J. Eng. Sci.,* **48,** 446–459.

Bock, H., 2001. Mont Terri Project. RA experiment: rock mechanics analyses and synthesis; data report on rock mechanics. Mont Terri Consortium, Tech. Rep. TR 2000/02.

Cheng, A.H.-D., 1997. Material coefficients of anisotropic poroelasticity, *Int. J. Rock. Mech. Min. Sci.,* **34,** 199–205.

Cook, J., 1999. The effects of pore pressure on the mechanical and physical properties of shales, *Oil Gas Sci. Technol.—Rev. IFP,* **54,** 695–701.

Detournay, E. & Cheng, A.H.-D., 1993. Fundamentals of poroelasticity, Chapter 5 in *Comprehensive Rock Engineering: Principles, Practice and Projects, Vol. II, Analysis and Design Method*, pp. 113–171, ed. Fairhurst, C., Pergamon Press.

Garboczi, E.J., 1998. *Finite Element and Finite Difference Programs for Computing the Linear Electric and Elastic Properties of Digital Images of Random Materials,* NIST.

Gens, A., Vaunat, J., Garitte, B. & Wileveau, Y., 2007. *In situ* behavior of a stiff layered clay subject to thermal loading: observations and interpretation, *Geotechnique,* **57,** 207–228

Healy, D., 2012. Anisotropic poroelasticity and the response of faulted rock to changes in pore-fluid pressure, in *Faulting, Fracturing and Igneous Intrusion in the Earth's Crust,* London Spec. Publ. Vol. 367, pp. 201–214, eds Healy, D., Butler, R.W., Shipton, Z.K. & Sibson, R.H., Geological Society.

Hornby, B.E., Schwartz, L.M. & Hudson, J.A., 1994. Anisotropic effective-medium modeling of the elastic properties of shales, *Geophysics,* **59,** 1570–1583.

Jahns, E., 2013. Geomechanical laboratory tests on Opalinus Clay cores from the bore hole Schlattingen SLA-1. Nagra Work Report NAB 13-18, Nagra, Wettingen, Switzerland.

Johnston, J.E. & Christensen, N.I., 1995. Seismic anisotropy of shales, *J. geophys. Res.,* **100,** 5991–6003.

Kanit, T., Forest, S., Gailliet, I., Mounoury, V. & Jeulin, D., 2003. Determination of the representative volume for random composites: statistical and numerical approach, *Int. J. Solids Struct.,* **40,** 3647–3679.

Keller, L.M., 2016. Pore geometry effects on elastic properties of Opalinus Clay, *Geophyiscs,* **81,** doi:10.1190/GEO2015-0452.1.

Keller, L.M., Hilger, A. & Manke, I., 2015. Impact of sand content on solut diffusion in Opalinus Clay, *Appl. Clay Sci.,* **112–113,** 134–142.

Keller, L.M., Holzer, L., Wepf, R. & Gasser, P., 2011. 3D Geometry and topology of pore pathways in Opalinus clay: implications for mass transport, *Appl. Clay Sci.,* **52,** 85–95.

Keller, L.M., Schuetz, P., Erni, R., Rossell, M.D., Lucas, F., Gasser, P. & Holzer, L., 2013a. Characterization of multi-scale microstructural features in Opalinus Clay, *Microporous Mesoporous Mater.*, **179,** 83–94.

Keller, L.M., Schuetz, P., Gasser, P. & Holzer, L., 2013b. Pore-space relevant for gas permeability in Opalinus Clay: statistical analysis of homgeneity, percolation and representative volume element (RVE), *J. geophys. Res.,* **118,** 1–14.

Madadi, M., Jones, A.C., Arns, C.H. & Knackstedt, M.A., 2009. 3D imaging and simulation of elastic properties of porous materials, *Comput. Sci. Eng.,* **11,** 65–73.

Meille, S. & Garboczi, E.J., 2001. Linear elastic properties of 2D and 3D models of porous materials made from elongated objects, *Modell. Simul. Mater. Sci. Eng.,* **9,** 371–390.

Monfared, M., Sulem, J., Delage, P. & Mohajerani, M., 2011. A laboratory investigation on thermal properties of the Opalinus Claytone, *Rock Mech. Rock Eng.,* **44,** 735–747.

Nagra, 2002. Projekt Opalinuston—Synthese der geowissenschafftlichen Untersuchungsergebnisse. Entsorgungsnachweis für abgebrannte Brennelemente, verglaste hochaktive sowie langlebige mittelaktive Abfälle. Nagra Tech. Rep. NTB 02-03, Nagra Wettingen, Switzerland.

Nagra, 2004. Effects of post-disposal gas generation in a repository for spent fuel, high-level waste and long-lives intermediate waste sited in the Opalinus Clay. Nagra Tech. Rep. NTB 04-06, Nagra, Wettingen, Switzerland.

Noiret, A., Giot, R., Bemer, E., Giraud, A. & Homand, F., 2011. Hydromechanical behavior of Tournemire argillites: measurement of the poroelastic parameters and estimation of the intrinsic permeability by oedometric tests, *Int. J. Numer. Anal. Meth. Geomech.,* **35,** 496–518.

Prasad, M., Kopycinska, M., Rabe, U. & Arnold, W., 2002. Measurement of Young's modulus of clay minerals using atomic force acoustic microscopy, *Geophys. Res. Lett.,* **29**(8), 13-1–13-4.

Reuss, A., 1929. Berechung der Fliessgrenze von Mischkristallen, *Z. Angew. Math. Mech.,* **9,** doi:0.1002/zamm.19290090104.

Revil, A. & Cathles, L.M., 1999. Permeability of shaly sands, *Water Resour. Res.,* **35,** 651–662.

Roberts, A.P. & Garboczi, E.J., 2000. Elastic properties of model porous ceramics, *J. Am. Ceram. Soc.,* **83,** 3041–3048.

Robinet, J.-C., Sardini, P., Coelho, D., Parneix, J.C., Prêt, D., Boller, E. & Altmann, S., 2012. Effects of mineral distribution at mesoscopic scale on solute diffusion in a clay-rich rock example of the Callovo-Oxfordian mudstone (Bure, France), *Water Resour. Res.,* **48,** W05554, doi:10.1029/2011WR011352.

Sarout, J. & Gueguen, Y., 2008a. Anisotropy of elastic wave velocities in deformed shales. Part 1—Modeling results, *Geophysics,* **73,** D91–D103.

Sarout, J. & Gueguen, Y., 2008b. Anisotropy of elastic wave velocities in deformed shales: Part 1—Experimental results, *Geophysics,* **73,** D75–D89.

Sarout, J., Esteban, L., Delle Piane, C., Maney, B. & Dewhurst, D.N., 2014. Elastic anisotropy of Opalinus Clay under variable saturation and triaxial stress, *Geophys. J. Int.,* **198,** 1662–1682.

Skempton, A.W., 1954. The pore pressure coefficients A and B, *Geotechnique,* **4,** 143–147.

Sone, H. & Zoback, M.D., 2013. Mechanical properties of shale-gas reservoir rocks—Part 1: Static and dynamic elastic properties and anisotropy, *Geophysics,* **78,** D381–D392.

Thomsen, L., 1986. Weak elastic anisotropy, *Geophysics,* **51,** 1954–1966.

Vanorio, T., Prasad, M. & Nur, A., 2003. Elastic properties of dry clay mineral aggregates, suspensions and sandstones, *Geophys. J. Int.,* **155,** 319–326.

Vernik, L. & Liu, X., 1997. Velocity anisotropy in shales: a petrophyscial study, *Geophysics,* **62,** 521–532.

Vernik, L. & Nur, A., 1992. Ultrasonic velocity and anisotropy of hydrocarbon source rocks, *Geophysics,* **57,** 727–735.

Wenk, H.-R., Voltolini, M., Mazurek, M., Van Loon, L.R. & Vinsot, A., 2008. Preferred orientation and anisotropy in shales: Callovo-Oxfordian shale (France) and Opalinus Clay (Switzerland), *Clays Clay Miner.*, **56,** 285–306.